Tribology International 146 (2020) 106181

Contents lists available at ScienceDirect

Tribology International

journal homepage: http://www.elsevier.com/locate/triboint

Auxiliary bearing squeeze film dampers for magnetic bearing supported rotors

Xiao Kang *, Alan Palazzolo, Wan Zhong

Texas A&M University, 3123 TAMU, College Station, TX, 77843, USA

ARTICLE INFO

Keywords:
Auxiliary bearing
Squeeze film damper
Magnetic bearing
Ball bearing

ABSTRACT

Auxiliary bearings (AB) support the rotor and protect the magnetic bearing (AMB) system when the AMB is disabled due to power loss or excessive loads. The paper demonstrates that installing a damping device along with the AB can yield extended AB fatigue life, protect the AMB, and reduce vibration, contact force and AB heating. A squeeze film damper (SFD) is an energy dissipation device that has been widely used in the turbo-machinery industry, and as demonstrated in the paper can also work effectively in combination with an AB. Usually, the SFD implements a supply groove to ensure adequate lubricant flow into the film lands. The supply groove can provide significant added mass coefficients and significantly influence the overall impedance of the SFD. Past literature has analyzed the transient response of the rotor dropping onto AB's with squeeze film dampers, none though have considered the influence of the SFD's center groove and its added mass effect on rotor's drop behavior. This paper develops a high fidelity finite element grooved SFD model considering the fluid inertia, and an effective groove clearance is used following the practice appearing in the literature. SFD force coefficients are benchmarked with results of a linear fluid inertia, bulk-flow model developed in the literature, before including them in the rotor – AB system model. The SFD model is integrated into a high fidelity nonlinear auxiliary bearing (angular contact ball bearing) model, which considers the movements, contact force, stress, and temperature of bearing balls, the inner race and outer race. The instantaneous reaction forces from the SFD are calculated with a finite element based solution of Reynold equation at each time step due to the intermittent and large sudden loads. The flexibility of the rotor is included utilizing a Timoshenko beam, finite element model. The fatigue life of the auxiliary bearing when integrated into the SFD is also calculated based on the rain flow counting method. The influence of the added mass of the SFD on the rotor's drop behavior is demonstrated showing that the added mass increases the contact force and peak temperature and reduces the fatigue life of the AB. Therefore, the added mass effect of the SFD should be considered to avoid over predicting the AB fatigue life. The influence of the SFD clearance on the rotor's drop behavior is also studied showing that an optimal clearance exists for increasing the AB fatigue life. Too small of a clearance will yield excessive damping making the effective stiffness too large, and causing high contact forces. Too large of a clearance lowers damping which may lead to a destructive backward whirl. This paper provides key guidelines for auxiliary bearing damper system design.

1. Introduction

Magnetic Bearings (MBs) systems rely on auxiliary bearings to protect the MBs and machinery in the event of a MB failure. A high-speed rotor dropping onto an auxiliary bearing (AB) can produce excessive contact forces and heating of the AB. Numerous studies have sought to accurately model the rotor drop events and improve the AB design for reducing peak contact force and AB heating. Gelin et al.'s [1] model included a flexible rotor dropping onto the AB but omitted friction forces between the rotor and AB. T. Ishii et al. [2] determined optimal damping for preventing backward whirl after the rotor drop utilizing a transient response – Jeffcott rotor model. Sun et al. [3] developed a detailed ball bearing type AB structural response model and later integrated the AB thermal model in Ref. [4] Lee et al. [5] developed a stress-based, high cycle fatigue HCF, AB life prediction model utilizing the rain flow cycle counting method. Sleeve type AB's are also popular in high-speed critical machines and rotordynamics response for drops onto sleeve type AB's has been investigated in various studies. Swanson et al. [6]

* Corresponding author.
E-mail addresses: kangxiao1990@tamu.edu (X. Kang), a-palazzolo@tamu.edu (A. Palazzolo), zhongwan0626@gmail.com (W. Zhong).

https://doi.org/10.1016/j.triboint.2020.106181
Received 11 January 2019; Received in revised form 31 October 2019; Accepted 10 January 2020
Available online 18 January 2020

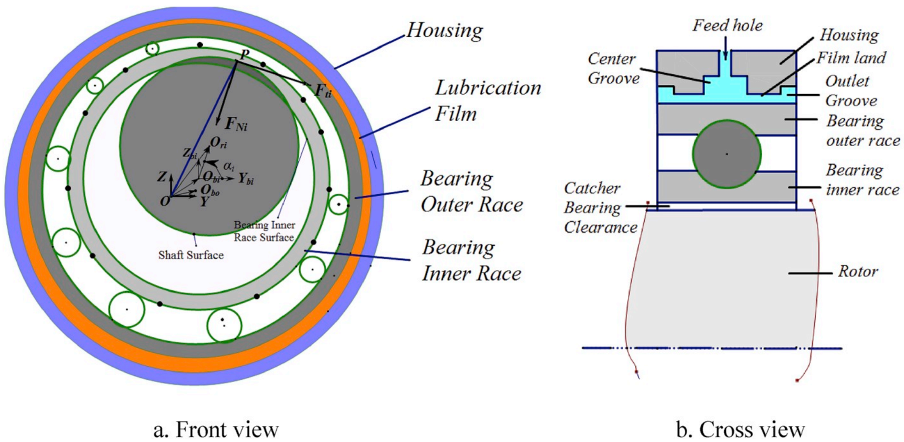

Fig. 1. Central Groove SFD integrated into an auxiliary bearing system.

numerically and experimentally [7] investigated rotor drop onto sleeve type ABs events. Kang et al. [8] extended the sleeve AB model to a 2D coupled elastic-thermal plane strain model where the 2D temperature and Von-Mises stress distributions were obtained.

The above AB models typically omitted high fidelity models of the dampers that are frequently installed with the ABs to mitigate excessive vibration and reduced AB life.

Some of the AB literature does consider damping devices such as the corrugated ribbon from Wilkes et al. [9] and the tolerance ring from Zhu et al. [10]. The squeeze film damper SFD is a commonly used energy dissipation device used to dampen rotating machinery vibration and is widely used in industry. Compared with the oil film bearings, which require an oil pump, heat exchangers, filters, considerable piping, etc. due to the need for high volume and high pressure flows, and continuous operation, often for a period of years, an AB SFD would only be active during the rare event of a rotor drop, typically in response to a power outage. Therefore the oil flow would be minimal, not only due to the non-rotation of the SFD, but also due to the short term operation of the AB in supporting the rotor during an unplanned shut-down event that would typically extend less than 30 s. We envision that the SFD would be supplied by a relatively inexpensive and compact oil accumulator charged with a similarly compact and low cost oil pump. Magnetic bearings are often used to preserve oil-free, contamination-free environments. The use of a SFD would not diminish this benefit of MBs since the SFD is not rotating and could be adequately sealed to prevent all oil leakage into the process flow. Finally, MBs have advantages over oil bearings even when oil is needed for a MB AB SFD such as lower drag power loss, adaptive control of stiffness and damping, etc.

The SFD typically employs a supply groove to ensure adequate lubricant flow into the film land. The geometry of the AB and SFD with central groove are illustrated in Fig. 1.

The fluidic forces from the groove were originally ignored due to their relative large depths, however test and theoretical results have shown large added mass coefficients in grooved SFD, i.e. Delgado [11]. This reference provides a linear fluid inertia bulk flow model for the analysis of the forced response of SFDs. The effective clearance is applied to replace the actual clearance of the groove based on the experimental data and the qualitative observations of the laminar flow pattern through annular cavities. Their simulation results of the SFD force coefficients correlated well with the experiments.

Some theoretical and experimental research has been performed with a SFD integrated into the AB system. Sun et al. [4] included an open-ended SFD and thermal analysis in an AB - rotor drop simulation study. However the groove of the SFD and the fluid inertia effect were ignored. Murphy et al. [12] integrated the SFD into the AB system of a magnetic bearing levitated flywheel, however a rotor drop simulation was not reported.

The present paper utilizes a finite element method (FEM) solution of Reynold's equation including the inertia force term to model a SFD with a center groove as shown in Fig. 1, which is similar with the linear bulk-flow model in Ref. [11]. As a preliminary benchmark, the SFD force coefficients including the damping and the added mass are correlated with [12]. The SFD model is integrated into the high fidelity nonlinear structural and thermal auxiliary bearing rotor drop model. Hertzian contact forces are applied between each bearing component, including the inner race, outer race, and each ball, in the auxiliary bearing model. Temperature variations and thermal expansions of each bearing component are included in the AB model. The rotor vibration is modeled with Timoshenko beam elements. A transient structural and thermal dynamics simulation of the AB and rotor is conducted for the case of the high-speed rotor dropping onto the ball bearing type AB through a clearance space. The AB is supported by a center grooved, squeeze film damper. The fatigue life of the AB is calculated by considering the resulting race stresses and using the rain flow counting method in Lee at al [5].

This paper investigates the influence of the added mass and the clearances of the SFD on the rotor drop behavior and provides guidelines for the SFD design in an AB application.

2. Center grooved SFD model

The pressure distribution in the SFD is obtained utilizing a finite element based solution of Reynold's equation using an effective clearance for the groove region [11]. The Reynold's equation for the film pressure of an incompressible fluid considering the temporal fluid inertia is

$$\frac{\partial}{\partial x}\left(\frac{h_i^3}{12\mu}\frac{\partial P}{\partial x}\right)+\frac{\partial}{\partial z}\left(\frac{h_i^3}{12\mu}\frac{\partial P}{\partial z}\right)=\frac{\partial h_i}{\partial t}+\frac{R\Omega}{2}\frac{\partial h_i}{\partial x}+\frac{\left(\rho h_i^2\right)}{12\mu}\frac{\partial^2 h_i}{\partial t^2} \tag{1}$$

where h_i represents the clearance in the ith section and the term $\frac{R\Omega}{2}\frac{\partial h}{\partial x}$ is zero since the rotational speed of the SFD inner race is zero. The pressure interpolation is

$$p(x,y)=\underline{N}^T\underline{p}_e \tag{2}$$

A linear triangular element is utilized so the shape function and nodal pressure vectors are

$$\underline{N}^T=(N_1 \quad N_2 \quad N_3) \tag{3}$$

$$\underline{P}_e^T=(P_{1e} \quad P_{2e} \quad P_{3e}) \tag{4}$$

Then, the Reynolds equation has the element level form

$$\underline{K}_e\underline{P}_e=\underline{S}_e+\underline{L}_e+\underline{I}_e \tag{5}$$

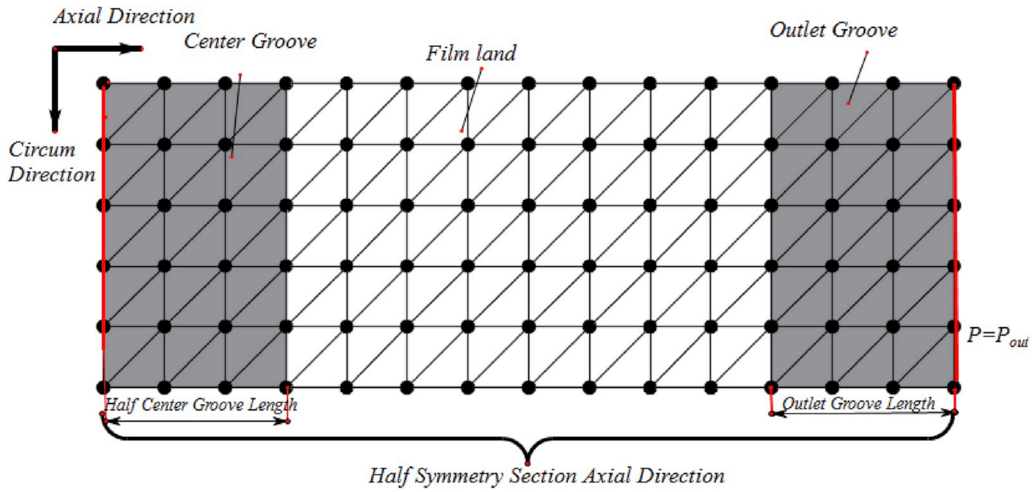

Fig. 2. Element mesh and boundary condition of the grooved SFD.

Table 1
SFD parameters in Ref. [11].

Radial Clearance in Damper	0.127 mm
Whirl Frequency	50 Hz
Damper Diameter	127 mm
Whirl Orbit radius	12 μm
Absolute Viscosity	2.8–3.1cp
Inlet Groove Length	6.36 mm
Discharge Groove Length	4.1 mm
Land Length	25.4 mm

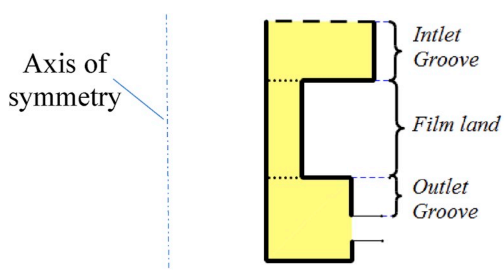

Fig. 3. Section view of the flow region of the SFD in Ref. [11].

where

$$(K_e)_{ij} = \left(\frac{h_e^3}{12\mu}\right)\int_{\Omega}\left(\frac{\partial N_i}{\partial x}\frac{\partial N_j}{\partial x}+\frac{\partial N_i}{\partial y}\frac{\partial N_j}{\partial y}\right)dxdy \ \mathrm{i}=1,2,3;\ \mathrm{j}=1,2,3 \tag{6}$$

and S_e represents the damping source term

$$(S_e)_i = -\frac{\partial h}{\partial t}*\int_{\Omega} N_i dxdy \tag{7}$$

The term I_e represents the fluid inertia:

$$(I_e)_i = -\left[\frac{(\rho h^2)}{12\mu}\frac{\partial^2 h}{\partial t^2}\right]_e * \int_{\Omega} N_i dxdy \tag{8}$$

The mesh of the SFD with a central groove is shown in Fig. 2.

A preliminary benchmark case was performed to ensure the accuracy of the isolated SFD component model prior to including it in the overall rotor/AB/SFD system model. The benchmark compared the present SFD model results to those of Delgado's end sealed SFD [11]. The parameters of the end seal SFD in Ref. [11] are shown in Table 1. The geometry is shown in.

The damping coefficient and added mass of the SFD are calculated with different effective clearance ratios of the groove in Fig. 3. The results are compared with the results from Ref. [11] linear bulk flow model, and show good agreement with a difference of less than 5%.

3. Combined Ab and grooved SFD sub-system

Fig. 1 illustrates a rolling element AB with a central groove, open-ended SFD. The AB outer race (ABOR) motion relative to the housing in Fig. 1 can be relatively large with respect to the clearance, and vary in a transient (non-periodic) manner due to impact or very high intermittent loading. This precludes the use of a linear dynamic coefficient model of the SFD forces, and instead requires a solution of Reynold's equation for the pressure distribution and resultant forces at each time step in the numerical integration. Inspection of the right-hand side of equation (10) shows that the instantaneous forces are attributable to an ABOR damping (velocity) and an ABOR inertia (acceleration) source term hence the total force may be represented as

$$F_{SFD} = F_{Inertia} + F_{Damping} \tag{9}$$

where $F_{Damping}$ is the SFD reaction force caused by the squeeze (velocity) effect and $F_{Inertia}$ is the reaction force only caused by the inertia (acceleration) effect. The inertia $F_{Inertia}$ is proportional to the acceleration of the ABOR, therefore

$$F_{Inertia} = \Lambda \ a_{\mathrm{CBOR}} \tag{10}$$

where Λ is an added mass type term. Note that by (1) Λvaries with the instantaneous film thickness and therefore varies with time, i.e. $\Lambda(t)$. The equation of motion of the ABOR is

$$\begin{bmatrix} M_{OR} & \\ & M_{OR}\end{bmatrix}\begin{bmatrix}\ddot{y}\\ \ddot{z}\end{bmatrix} = \begin{bmatrix}F_{stiffy}+F_{bally}+F_{dampingy}\\ F_{stiffz}+F_{ballz}+F_{dampingz}\end{bmatrix} + \begin{bmatrix}\Lambda_{yy} & \Lambda_{yz}\\ \Lambda_{zy} & \Lambda_{zz}\end{bmatrix}\begin{bmatrix}\ddot{y}\\ \ddot{z}\end{bmatrix} \tag{11}$$

where F_{stiffy} represents the force acted by the supporting device of the SFD, F_{bally} represents the summation of the forces acted by all the bearing balls, $F_{dampingx}$ is the force purely caused by the damping of the SFD, and Λ_{yy}, etc. are the transient added mass terms. Moving the added mass terms to the left side of the equation (16) forms equation, which does not have acceleration terms on its right hand side.

$$\begin{bmatrix} M_{OR}-\Lambda_{yy} & -\Lambda_{yz}\\ -\Lambda_{zy} & M_{OR}-\Lambda_{zz}\end{bmatrix}\begin{bmatrix}\ddot{y}\\ \ddot{z}\end{bmatrix} = \begin{bmatrix}F_{stiffy}+F_{bally}+F_{dampingy}\\ F_{stiffz}+F_{ballz}+F_{dampingz}\end{bmatrix} \tag{12}$$

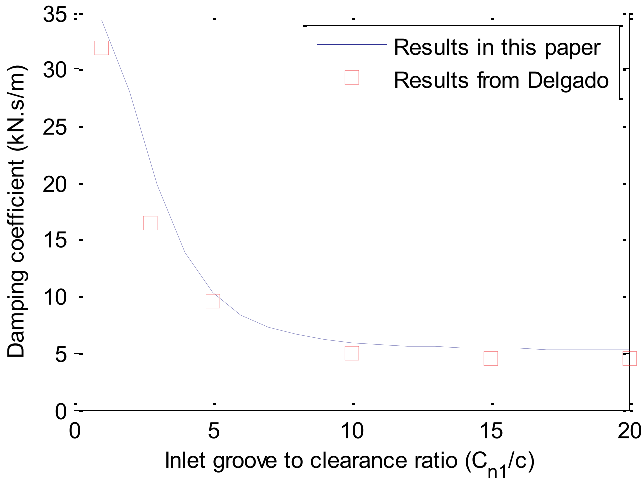

a. Damping coefficient

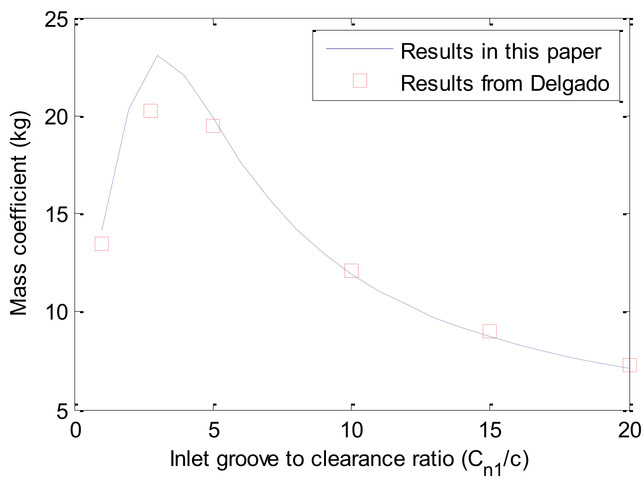

b. Added Mass

Fig. 4. Damping coefficient and added mass for different clearance ratios.

4. Ab system modeling

Ball bearings are commonly used as AB's in magnetic bearing applications. The contact forces between bearing races and balls are included in the following detailed model of the AB, and are treated with nonlinear, Hertzian contact representations. The nonlinear auxiliary bearing model is based on references [4,5]. Fig. 4 illustrates the geometry of the angular contact ball bearing AB.

The symbols $X-Y-Z$ represents the global coordinates, and $X_j-Y_j-Z_j$ represents the local coordinates with respect to the jth bearing ball, in Fig. 4. The transformation between the local coordinate and the global coordinate is

$$\begin{bmatrix} x_j \\ y_j \\ z_j \end{bmatrix} = \begin{bmatrix} 1 & 0 & 0 \\ 0 & \cos\phi_j & \sin\phi_j \\ 0 & -\sin\phi_j & \cos\phi_j \end{bmatrix} \begin{bmatrix} x \\ y \\ z \end{bmatrix} \tag{13}$$

The coordinate transformation matrix from global coordinates to the jth ball local coordinates is

$$T_j = \begin{bmatrix} 1 & 0 & 0 \\ 0 & \cos\phi_j & \sin\phi_j \\ 0 & -\sin\phi_j & \cos\phi_j \end{bmatrix} \tag{14}$$

The forces between the balls and the inner and outer races, are calculated in the respective ball local coordinates and then transformed to global coordinates.

Fig. 5 shows the kinematic and thermal deformation displacements for the inner and outer races and the jth ball, where l_{oe} is the initial distance between the outer race groove center and the bearing ball center, l_{oi} is the distance between the inner race groove center and the ball center, α_0 is the initial contact angle, α_{oe} is the contact angle between the outer race and the ball after the external load is applied, α_{oi} is the contact angle between the inner race and the ball after the external load is applied, and ε_b, ε_e, ε_i are the thermal expansions of the ball, outer and inner race, respectively.

The geometric relationships among these displacements and lengths are:

$$l_{oi} = r_i - \frac{D}{2} \tag{15}$$

$$l_{oe} = r_e - \frac{D}{2} \tag{16}$$

$$\tan\alpha_{oi_j} = \frac{l_{oi}\sin\alpha_o - v_x + u_x}{l_{oi}\cos\alpha_o - v_r + u_r + \varepsilon_i} \tag{17}$$

$$\tan\alpha_{oe_j} = \frac{l_{oe}\sin\alpha_o - w_x + v_x}{l_{oe}\cos\alpha_o - w_r - \varepsilon_e + v_r} \tag{18}$$

$$l_{i_j} = \varepsilon_b + \sqrt{(l_{oi}\sin\alpha_o - v_x + u_x)^2 + (l_{oi}\cos\alpha_o - v_r + u_r + \varepsilon_i)^2} \tag{19}$$

$$l_{\varepsilon_j} = \varepsilon_b + \sqrt{(l_{oe}\sin\alpha_o - w_x + v_x)^2 + (l_{oe}\cos\alpha_o - w_r - \varepsilon_e + v_x)^2} \tag{20}$$

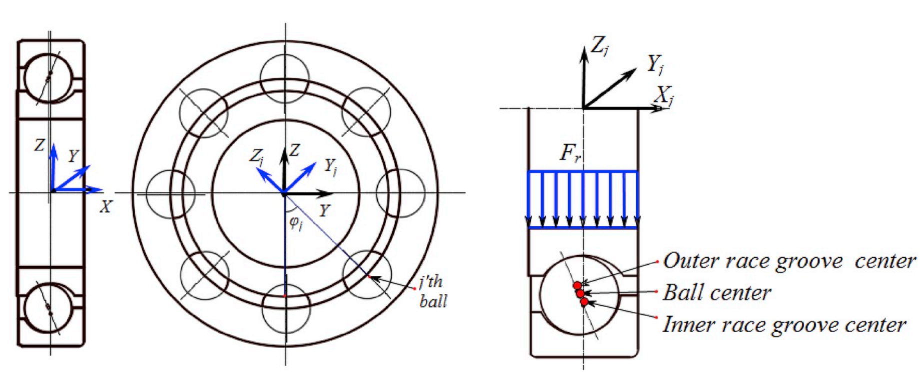

(a) (b)

Fig. 5. (a) Auxiliary bearing geometric and local coordinates with respect to jth ball. (b) Auxiliary bearing geometric relationship for jth ball in its local coordinates.

Table 2
Values of z and y vs. ball bearing type.

Ball Bearing Type		Z	y
Deep groove	α = 0°	0.0007	0.55
Angular contact	α = 30°	0.001	0.33
Angular contact	α = 40°	0.001	0.33
Thrust	α = 90°	0.001	0.33

Table 3
Values of fo vs. Bearing Type and Lubrication [13].

Bearing Type	Oil Mist	Oil Bath or Grease	Oil Bath* or Oil Jet
Deep groove ball	0.7–1	~2	3–4
Self-aligning ball		5	
Thrust ball			
Angular contact ball			
single row	1	3	6
double row	2	6	9

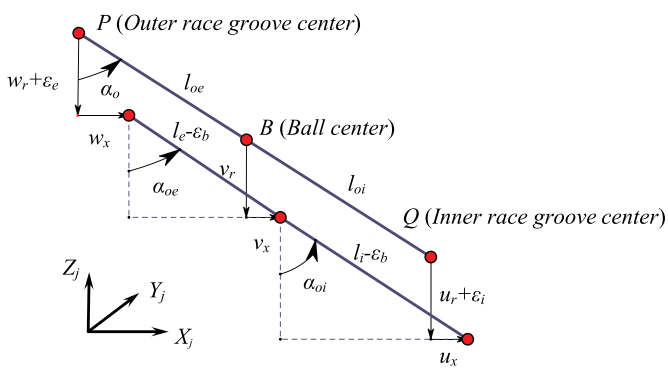

Fig. 6. Kinematic and thermal deformation displacements of the races and jth ball.

The penetration δ_{i_j} between the inner race and the jth bearing ball is

$$\delta_{i_j} = l_i - l_{oi} \tag{21}$$

The penetration δ_{e_j} between the outer race and the jth bearing ball is

$$\delta_{e_j} = l_e - l_{oe} \tag{22}$$

The contact force between the inner race and the jth ball is

$$Q_{i_j} = k_i \delta_i^{\frac{3}{2}} \left(\frac{3}{2}\beta\delta_i + 1\right) \tag{23}$$

where the term k_i depends on the geometry and material of the ball and races. Similarly, the contact force between the outer race and the jth ball is

$$Q_{e_j} = k_e \delta_e^{\frac{3}{2}} \left(\frac{3}{2}\beta\delta_e + 1\right) \tag{24}$$

The equation of motion of the bearing inner race is

$$\begin{bmatrix} 2m_{bi} & 0 & 0 \\ 0 & 2m_{bi} & 0 \\ 0 & 0 & 2m_{bi} \end{bmatrix} \begin{bmatrix} \ddot{x}_{bi} \\ \ddot{y}_{bi} \\ \ddot{z}_{bi} \end{bmatrix} = \begin{bmatrix} F_x \\ F_{ky} \\ F_{kz} \end{bmatrix} + \sum_{j=1}^{n} \left(T_j^{-1} \begin{bmatrix} Q_{ex_j} \\ Q_{ey_j} \\ Q_{ez_j} \end{bmatrix} \right) \tag{25}$$

where F_x , F_{ky} *and* F_{kz} are contact forces between the rotor and the inner race in three different directions, which will be explained in a later section, and where Q_{ix_j}, Q_{iy_j}, Q_{iz_j} are projections of contact forces from bearing inner race in global x, y and z directions.

The equation of motion of the outer race is

$$\begin{bmatrix} 2m_{bo} & 0 & 0 \\ 0 & 2m_{bo} & 0 \\ 0 & 0 & 2m_{bo} \end{bmatrix} \begin{bmatrix} \ddot{x}_{bo} \\ \ddot{y}_{bo} \\ \ddot{z}_{bo} \end{bmatrix} = \sum_{j=1}^{n} \left(T_j^{-1} \begin{bmatrix} Q_{ex_j} \\ Q_{ey_j} \\ Q_{ez_j} \end{bmatrix} \right) + \begin{bmatrix} F_{stiffx} + F_{dampingx} \\ F_{stiffy} + F_{dampingy} \\ F_{stiffz} + F_{dampingz} \end{bmatrix} \tag{26}$$

The equation of motion for the jth ball is

$$\begin{bmatrix} m_b & 0 & 0 \\ 0 & m_b & 0 \\ 0 & 0 & m_b \end{bmatrix} \begin{bmatrix} \ddot{x}_{b_j} \\ \ddot{y}_{b_j} \\ \ddot{z}_{b_j} \end{bmatrix} = T_j^{-1} \begin{bmatrix} Q_{ix_j} - Q_{ex_j} \\ Q_{iy_j} - Q_{ey_j} \\ Q_{iz_j} - Q_{ez_j} \end{bmatrix} - T_j^{-1} \begin{bmatrix} 0 \\ 0 \\ F_{c_j} \end{bmatrix} \tag{27}$$

where F_{c_j} is the centrifugal force for the jth ball.

The drag torque between races and balls in auxiliary bearings, can also greatly influence the dynamic and thermal behavior of the rotor-bearing system. Large drag torques may lead to sizable heat generation and resulting failure of the ABs. There are two dominant bearing drag torques based on reference [13]. The first drag torque from ABs is as follow:

$$T_{dl} = f_1 F_\beta d_m \tag{28}$$

d_m is the pitch diameter of the bearing.
F_β is depended on the applied load. For angular ball bearings, the F_β is calculated as follow.
$F_\beta = \max(0.9F_z \cot\alpha - 0.1F_{r'} \quad F_r)$
F_r is the radial load, F_z is the axial load.
f_1 for the rolling bearing, f_1

$$f_1 = z(F_s/C_s)^y \tag{29}$$

F_s is the static equivalent load.
C_s is the basic static load rating
The value of z and y are listed in Table 2.

The second type of drag torque is obtained experimentally from Palmgren [13].

$$T_{dv} = 10^{-7} f_0 (v_0 n)^{2/3} {d_m}^3 \ for\ v_0 n > 2000 \tag{30}$$

$$T_{dv} = 160 \times 10^{-7} f_0 {d_m}^3 \ for\ v_0 n \le 2000 \tag{31}$$

where.

v_0 is the kinematic viscosity of the lubricant in centistokes,
f_0 depends on the type of bearing and method of lubrication,
n is the inner race angular velocity in units of rpm, and
f_0 is shown in Table 3 for different lubricant condition

Therefore, the equation of motion of the angular degree of freedom of the auxiliary bearing inner race is

$$I_{bi}\ddot{\theta}_x = F_{ti}(R_{bi} + \Delta_{ri} - cr) - T_{dv} - T_{dl} \tag{32}$$

where I_{bi} is the moment of inertia of the AB inner race, $\ddot{\theta}_x$ is the angular acceleration in the axial direction, T_{dv}, T_{dl} are the drag torques of the ball bearing, which can be found in equation, , and, cr is the clearance between the rotor and the AB, and the other parameters in equation can be found in Fig. 6.

5. Rotor – Ab contact model

As shown in Fig. 6, assume that the rotor node number at the AB location is k.

The contact forces acting on the rotor due to AB inner race contact are

$$F_{ky} = -F_{Nk}\cos\alpha_i + F_{tk}\sin\alpha_k \tag{33}$$

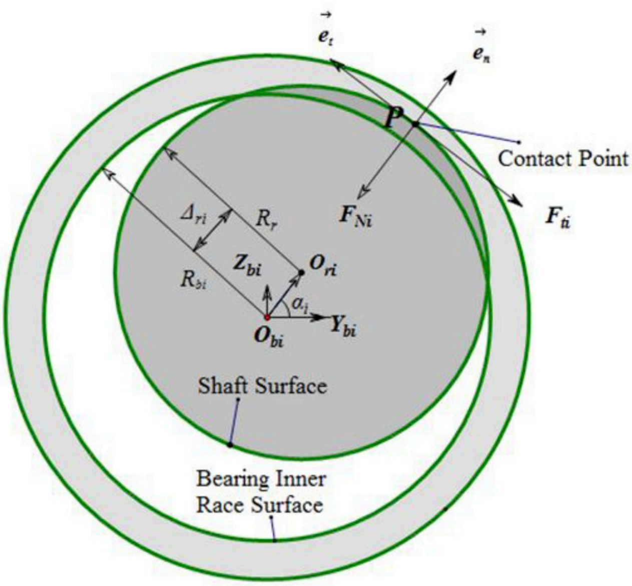

Fig. 7. Contact between the rotor and the auxiliary bearing inner race.

$$F_{kz} = -F_{Nk}\sin\alpha_k - F_{tk}\cos\alpha_k \tag{34}$$

The torque on the rotor at the AB location is

$$T_{\theta_x k} = -R_{rk}F_{tk} \tag{35}$$

where R_{rk} is the radius of the rotor at the AB's location.

The force between the rotor and the AB inner race is treated as a Hertzian line contact [3].

$$F_{Nk} = K_l\delta^{\frac{10}{9}}\left(1+\frac{3}{2}\beta\dot{\delta}\right) \tag{36}$$

where K_l can be calculated from Ref. [3] as

$$K_l = \frac{0.39^{\frac{10}{9}}}{l}\left(\frac{4(1-v_1^2)}{E_1}+\frac{4(1-v_2^2)}{E_2}\right) \tag{37}$$

The friction force between the AB inner race and the rotor becomes

$$F_{tk} = \mu_r F_{rk}, \quad (v_{rel}>0) F_{rll}, \qquad (v_{rel}=0) \quad -\mu_r F_{rk}, \quad (v_{rel}<0) \tag{38}$$

A Stribeck friction model is employed where

$$\mu_r = -\frac{2}{\pi}\arctan(\varepsilon_f v_{rel})\left[\frac{\mu_s-\mu_d}{1+\delta_f|v_{rel}|}+\mu_d\right] \tag{39}$$

$$F_{tk} = -\mu_r F_{Nk}, \quad V_{rel}\neq 0 \tag{40}$$

where ε_f determines the steepness of the approximation function, δ_f is a positive number that determines the rate at which the static friction coefficient approaches the dynamic friction coefficient with respect to relative velocity. The term "$-\frac{2}{\pi}\arctan(\varepsilon_f vel_{rel})$" has a similar function to the "sign" function, but provides improved numerical stability of the system simulation and agrees well with experimental data according to Ref. [14]. The relative tangential velocity of the contact point P, v_{rel}, as shown in Fig. 6, on the rotor is

$$\begin{aligned} v_{rel} = & -\dot{y}_i\sin\alpha_i + \dot{z}_i\cos\alpha_i + R_r\dot{\theta}_{xi} \\ & -(-\dot{y}_{bi}\sin\alpha_i + \dot{z}_i\cos\alpha_i + (R_{bi}+\Delta_{ri}-cr)\dot{\theta}_{bxi}) \end{aligned} \tag{41}$$

The Stribeck friction factor model provides a smooth transition between static and sliding friction and is plotted vs. the relative tangential velocity in Fig. 7. The parameter values utilized in Fig. 7 are $\varepsilon_f = 10000$, $\delta_f = 1$, $\mu_s = 0.2$ and $\mu_d = 0.15$.

The rotor is modeled with Timoshenko beam finite elements and has the general form

$$M\ddot{X} + [C+\Omega G]\dot{X} + KX = F \tag{42}$$

where M, C, G and K are the mass, damping, gyroscopic and stiffness matrices of the rotor and Ω is its angular velocity. The vector X contains the nodal degree of freedom of the rotor and F is the load vector including the weight, mass imbalance forces and the nonlinear auxiliary bearing contact forces. Each beam node has six degrees of freedom, including three translations, and three rotations. A fourth-order Runge-Kutta numerical integration method is used to solve (43) given initial conditions.

6. Ab thermal model

Large amounts of heat may be generated due to the friction after the rotor drops onto the AB. This can cause thermal expansion of the bearing inner race, balls, and outer race. Such a process can increase the preload of the bearing and consequently generate more heat, possibly leading to a "thermal runaway" condition. There are three major heat sources that occur when the rotor drops onto the auxiliary bearing:

1) Friction torque due to the external steady loads
2) Viscous friction torque
3) Friction between the rotor and the AB inner race

Here the heat generated in the SFD are ignored.

Heat source (1) results from friction between the ball bearing's components which can be calculated by the drag torque formula [13].

$$T_{dl} = f_1 F_\beta d_m \tag{43}$$

The corresponding thermal power loss is

$$H_p = T_{dl}\ \omega_i \tag{44}$$

where ω_i is the rotational speed of the bearing inner race. Heat source (2) is caused by the friction between bearing components and the lubricant and is expressed by

$$H_v = T_{dv}\omega_i \tag{45}$$

The third heat source is the sliding friction between the shaft surface and the bearing inner race

$$H_s = F_t v_{rel} \tag{46}$$

The heat flux is assumed to be uniformly distributed in the radial direction and is symmetric in the axial direction. This permits the use of a computationally efficient one-dimensional, lumped thermal mass, radial heat transfer equation. Thermal resistances are included to account for heat conduction between the lumped thermal masses. Further assumptions for the thermal bearing model include.

a) Heat sources are located on the balls, the inner race, and outer race.
b) Heat sources are shared evenly between components if occurring at a contact point between the 2 components
c) The ball bearing is modeled with lumped thermal masses
d) Each lumped thermal mass has a uniform temperature

The geometry and heat transfer network is shown in Fig. 8.

The thermal resistance of the squeeze film damper is

$$R_{SFD} = \frac{\ln((r_{sfd}+c_{film})/r_{sfd})}{2\ \pi\ k_{sfd}\ L_{film}} + \frac{\ln((r_{sfd}+c_{groove})/r_{sfd})}{2\ \pi\ k_{sfd}\ L_{groove}} \tag{47}$$

Other thermal resistances are calculated based on [5]. The

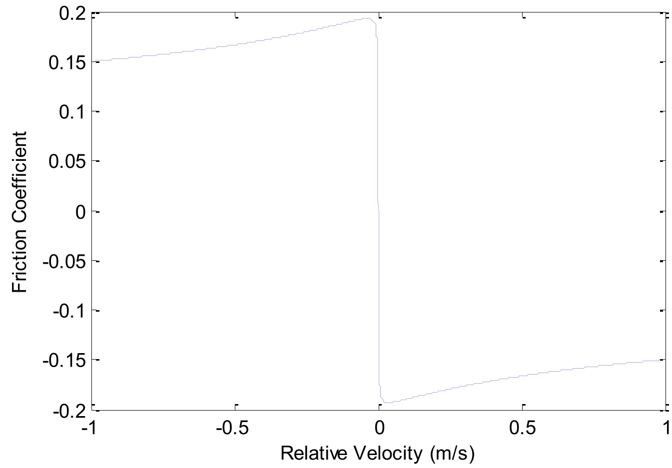

Fig. 8. Stribeck model friction coefficient vs. tangential relative velocity.

differential equation of the AB heat transfer model is

$$M_c\ \dot{T}_c = A_c\ T_c + H \tag{48}$$

where M_c is the thermal mass matrix, T_c is the nodal temperature vector, A_c is the matrix of thermal resistances, and H is the heat source vector. The thermal expansion of the auxiliary bearing system is included in the AB model based on reference [5]. The radial thermal expansion of the bearing outer race is

$$\varepsilon_e = \frac{\xi_e}{3}\ \frac{(1+\upsilon_e)\ r_e}{r_e + r_h}\ [\Delta T_{Le}(2r_e + r_h) + \Delta T_h(2r_h + r_e)] \tag{49}$$

The radial thermal expansion of the bearing inner race is

$$\varepsilon_i = \frac{\xi_i}{3}\ (1+\upsilon_i)\ r_i\ [\Delta T_s + \Delta T_{Li}] \tag{50}$$

The radial thermal expansion of the bearing balls is

$$\varepsilon_b = \xi_b\ r_b\ \Delta T_b \tag{51}$$

7. Ab life prediction

A possible fatigue failure mechanism for a rolling element bearing is the excessive orthogonal shear stress τ_o occurring at a location slightly below a surface that is subjected to a concentrated, perpendicular contact force. This stress is given by

$$\frac{2\tau_0}{\sigma_{\max}} = \frac{\sqrt{2(t-1)}}{t(t+1)} \tag{52}$$

where t is an auxiliary parameter determined by the elliptic contact region as shown in equation and Fig. 9.

The quantity $\sigma_{\max}$ is defined by:

$$\sigma_{\max} = -\frac{3Q}{2\pi ab} \tag{53}$$

where Q is the load between inner race and ball or outer race and ball, a, b are the semi-major and the semi-minor axes of the projected elliptical area. They can be calculated by Hertzian contact theory [13]. Additionally, the relationship between the b/a and the auxiliary parameter t is shown in

$$\frac{b}{a} = \sqrt{(t^2-1)(2t-1)} \tag{54}$$

Additionally, surface shear stress also contributes much to the fatigue failure of the AB. It is

$$\tau_{surface} = \mu_{ball}\sigma \tag{55}$$

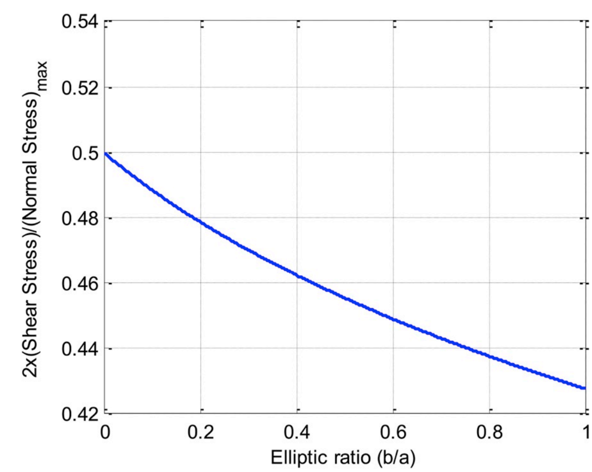

Fig. 10. Sub-surface shear stress ratio $\tau_0/\sigma_{\max}$ vs. ellipse axis ratio.

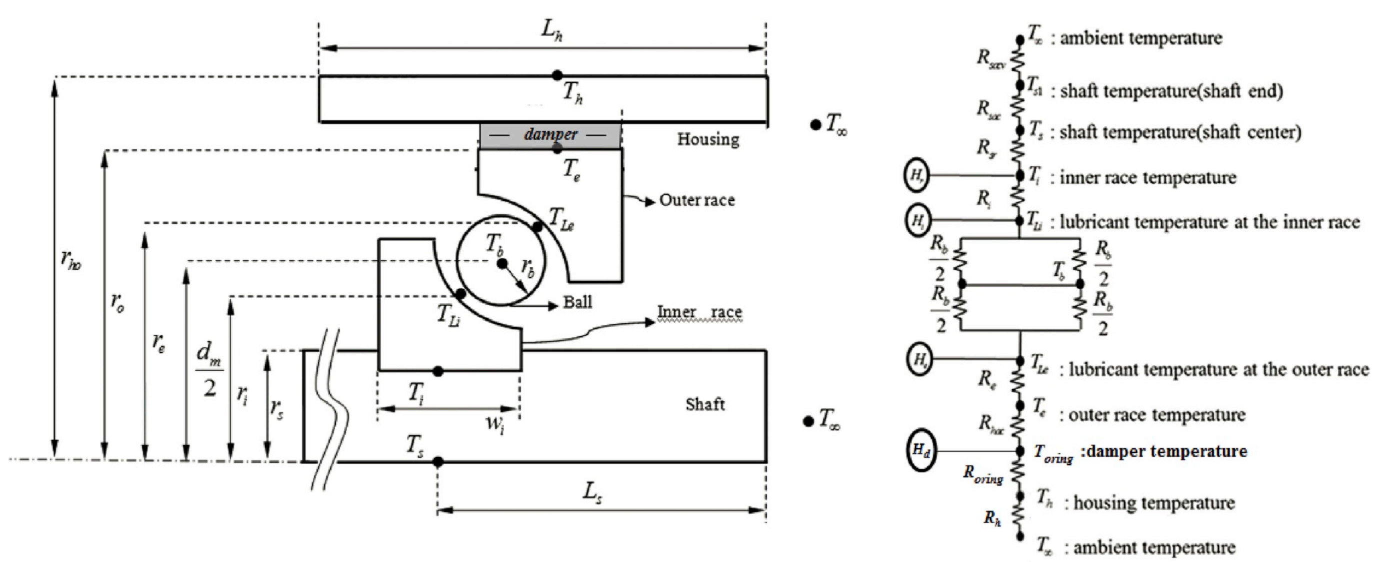

Fig. 9. Heat transfer model for AB and SFD.

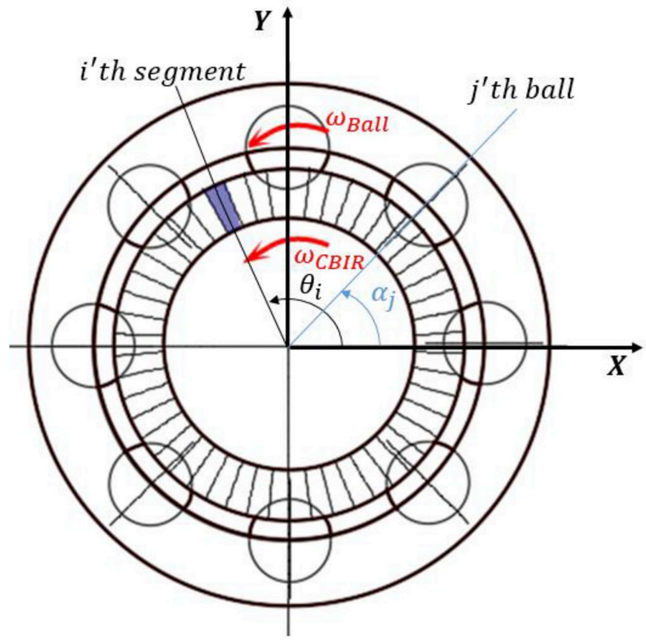

Fig. 11. Contact condition of the bearing balls and each segment of the ABIR.

Table 4
Rotor and AM model parameters.

Rotor drop spin speed	20,000RPM
Dynamic friction coefficient	0.35
Static friction coefficient	0.45
Air gap	0.3 mm
Bearing bore diameter	80.0 mm
Bearing outer diameter	125.00 mm
Bearing width	22.0 mm
Pitch diameter	110.mm
Ball diameter	19.05 mm
Number of balls	10
Ambient temperature	25 °C
Number of ABIR segments for the fatigue life calculation	100

Table 5
Squeeze film damper parameters.

Radial clearance in damper (mm)	0.254
Absolute viscosity (kg/s)	3.1522 kg/s
Damper diameter (mm)	127
Damper total length/damper diameter	0.5
Inlet groove length (mm)	12.7
Fluid density (kg/m^3)	785
Effective groove clearance/film clearance	20

where μ is the friction coefficient between ball and races and σ is the normal stress. The value of μ is typically 0–0.2, here it set to be 0.2 [5].

Based on simulation results, the contact stresses on the AB inner race IR are larger than that on the AB outer race. Therefore, here we use the fatigue life of the AB inner race to represent the fatigue life of the AB. To accurately obtain the AB inner race's fatigue life, the AB inner race is separated into segments in the circumferential direction, then the fatigue life of each segment will be calculated and the lowest one will be the fatigue life of the AB inner race. The stress is directly obtained from the contact stress between the ABIR and each bearing ball when calculating the shear stress of each segment. There is an assumption that the contact stresses acting on each segment are assumed to act on the center point of the segment. The results become less conservative when the segment number is increased due to the reduced number of impacts in smaller segments.

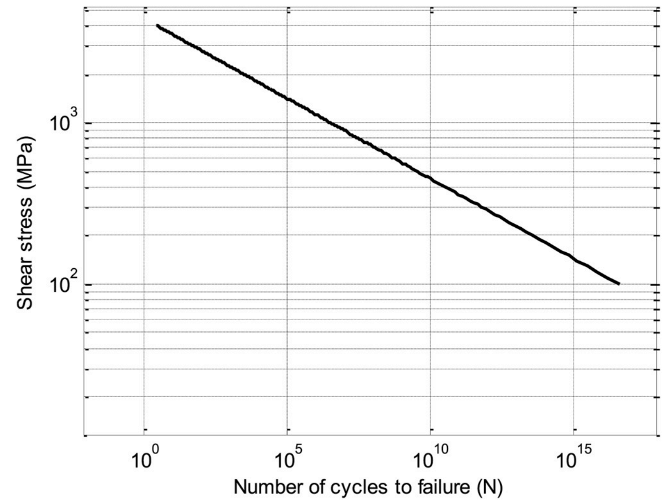

Fig. 12. S–N curve [5].

Let θ_{ABIR} be the rotated angle of the ABIR, n_{seg} to be the total segment number. α_{cage} is the rotated angle of the AB cage, θ_i be the initial circumferential location of the center point of each segment. α_j is the initial circumferential location of the jth ball, which can be found in Fig. 10. F_{segi} to be the contact force on the center point of each segment of the ABIR. F_{ballj} to be the contact force between the jth ball and the ABIR. Therefore, the contact force of each segment can be determined as follow:

$$F_{segi} = \begin{cases} F_{ballj}, \quad if \quad abs\left(\theta_{ABIR} + \theta_i - \alpha_{cage} - \alpha_j\right) \leq \dfrac{2\pi}{2n_{seg}} \\ 0 \quad if \quad abs\left(\theta_{ABIR} + \theta_i - \alpha_{cage} - \alpha_j\right) \geq \dfrac{2\pi}{2n_{seg}} \end{cases} \tag{56}$$

Fig. 10 shows the contact condition of the bearing balls and each segment of the ABIR.

As described in Ref. [15], fatigue damage under rolling contact conditions is caused purely by the action of shear stresses, with the mechanism of failure similar to the torsional fatigue. Therefore, both of the relationships between fatigue cycles and the shear forces are based on the torsional fatigue test data.

The Rainflow counting method is applied to calculate the fatigue life of the auxiliary bearing as presented in Ref. [3]. The cumulative damage D and number of cycles N to failure are determined using a histogram of cycle ranges and Miner's rule

$$D = \frac{n_1}{N_1} + \frac{n_2}{N_2} + \cdots = \sum_i \frac{n_i}{N_i} \geq 1 \tag{57}$$

where n_i is the number of applied cycles and N_i is the number of cycles to failure at a certain stress amplitude τ_i. The critical cumulative damage value of D is chosen to be 1. AB life is estimated from

$$life = \frac{1}{\sum_i \frac{n_i}{N_i}} \tag{58}$$

The S–N curve being used for the fatigue life calculation is shown in Fig. 11 based on reference [5].

8. Numerical example: Sfd benefits

This section provides a numerical example to illustrate the preceding analysis and demonstrate the benefits of installing a central groove SFD into the AB system. The SFD model includes fluid inertia effects and

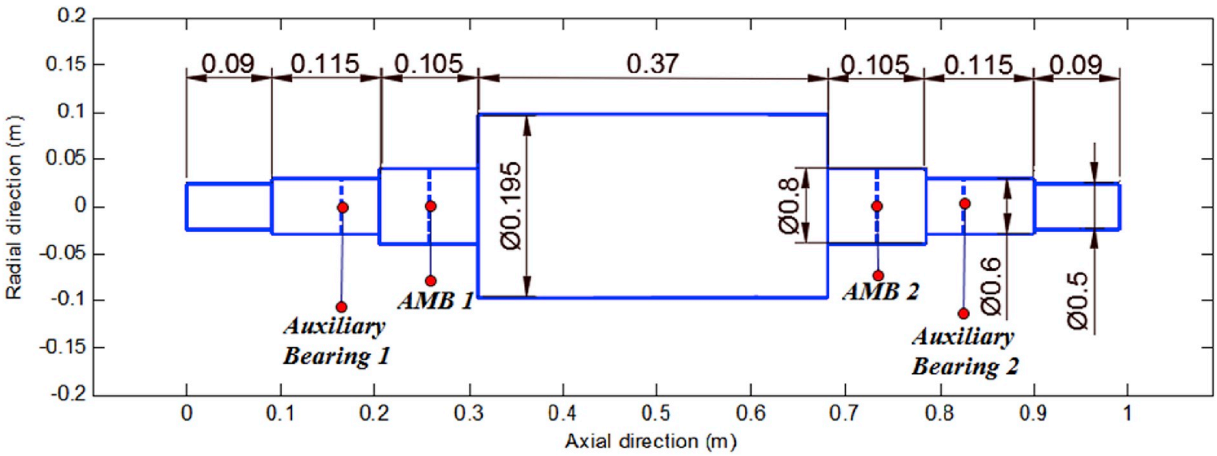

Fig. 13. Geometry of the example rotor and FE mesh (dashed).

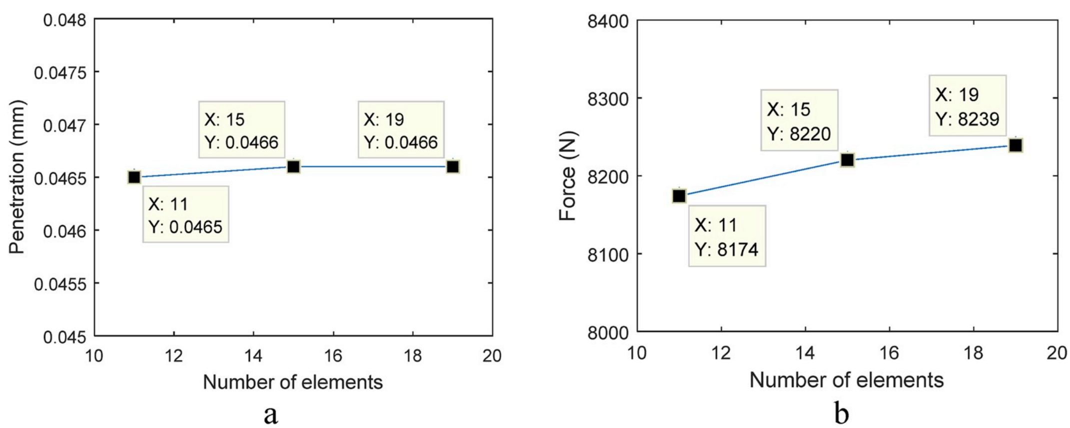

Fig. 14. Grid independence study for the flexible rotor, a. maximum radial penetration, b. maximum contact force.

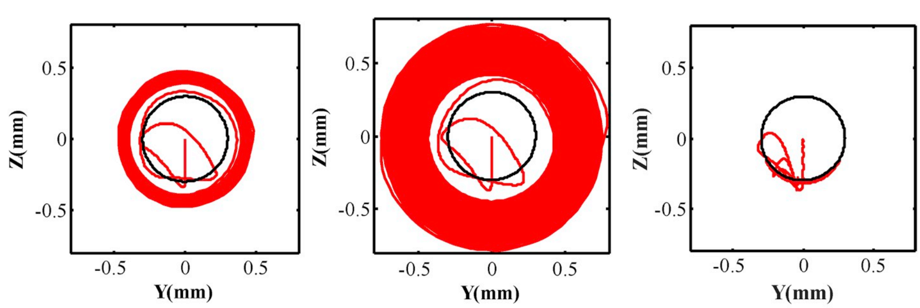

a. Without SFD, fixed ABOR b. Without SFD, soft support c. with SFD

Fig. 15. Rotor drop orbit plots.

utilizes a FEM model of the oil film to calculate the instantaneous forces exerted on the AB housing by the SFD. These forces are utilized in a nonlinear, transient, numerical integration of the system equations of motion.

The SFD is supported on an anti-rotation spring (squirrel cage) which also provides a radial stiffness of 1e8N/m. All drop tests occur at a rotational speed of 20,000 rpm. By comparison, the critical speed of the rotor supported by the squirrel cage stiffness is 11,690 rpm. The AB clearance for the example is 0.3 mm. The simulation parameter values for the rotor and the auxiliary bearing are given in Table 4. The parameter values for the squeeze film damper are provided in Table 5.

Simulations are performed with the AB outer raced fixed, and with it flexibly mounted on a SFD, in order to demonstrate the benefit of the SFD on force and vibration reduction and extension of AB life. A third AB support case is also presented: a soft mounted AB supported by the same squirrel cage stiffness as with the SFD but without the SFD.

The friction coefficient between the rotor and the AB inner race is 0.35, since this value precipitates backward whirl, providing a vibration control challenge for the SFD. Fig. 12 shows the geometry of the example rotor with the catcher bearing locations. The flexible rotor model has a total of 11 elements, which was arrived at based on a grid independence study, as illustrated in Fig. 11 for maximum radial penetration between the rotor and AB system and maximum contact force during the first impact. The difference between contact force when using 11 elements

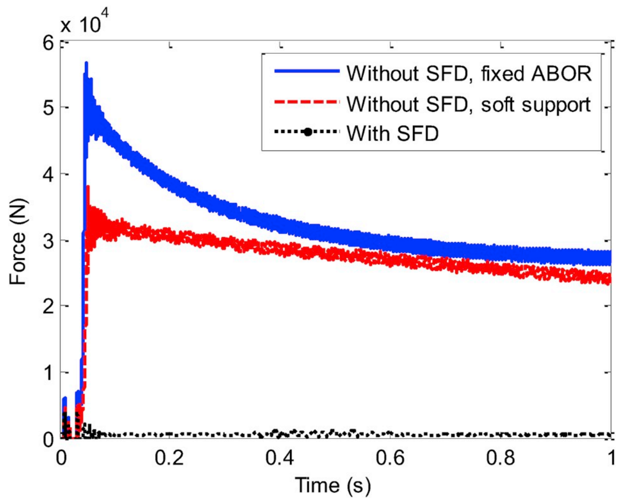

Fig. 16. Normal contact forces between the shaft and AB with and without the SFD.

and 19 elements is within 1%. Eleven 11 elements were used to model the flexible rotor in a computationally economical manner (see Fig. 14) (see Fig. 13).

Rotor orbits with and without the SFD are shown in Fig. 15. The black circles in Fig. 15 represents the unloaded clearance circle of the AB.

Fig. 15 shows that the AB mounted on the squirrel cage stiffness without the SFD results in a severe backward whirl BW. The BW is totally eliminated with the addition of the SFD.

Fig. 16 shows that the AB mounted on the squirrel cage stiffness without the SFD results in very large contact forces between the shaft and the AB inner race due to BW. The large sustained contact forces are totally eliminated with the addition of the SFD. Fixing the AB outer race to ground results in larger sustained contact forces but smaller vibration amplitude compared with the case when the AB is supported with the squirrel cage stiffness. Fig. 17 shows the shear stresses on the segment of the ABIR with the lowest fatigue life in different supporting conditions.

The large sustained stresses are virtually eliminated with the addition of the SFD. Fixing the AB outer race to the ground results in relatively higher stresses compared with the case with softer support. The detail stress cycle counts are shown in Fig. 18.

Fig. 19 shows the temperature variation of the AB balls with and without the SFD. The results show that the increase in temperature is more than 10 times larger for the without SFD case, compared with the with SFD case. Fixing the AB outer race to ground results in higher temperature compared with the case with soft supports.

In summary, this example shows that including the SFD results in significant reductions in contact stress, contact force, temperature rise and vibration amplitudes. The example also shows that fixing the AB outer race to ground results in higher contact forces and temperature increment.

9. Film clearance influence on SFD effectiveness

The preceding example demonstrated the benefits of a properly designed SFD on reducing vibration, contact forces, race stress and ultimately AB fatigue life. This section treats the oil film clearance as a design variable for properly designing the SFD. The clearance of the SFD film land is varied from 0.127 mm to 0.381 mm while the effective groove clearance ratio between the groove land and the film land is held constant at 20. Fig. 20 shows the rotor orbit with various SFD clearances. Fluid inertia is included in the film model and the zero clearance (no

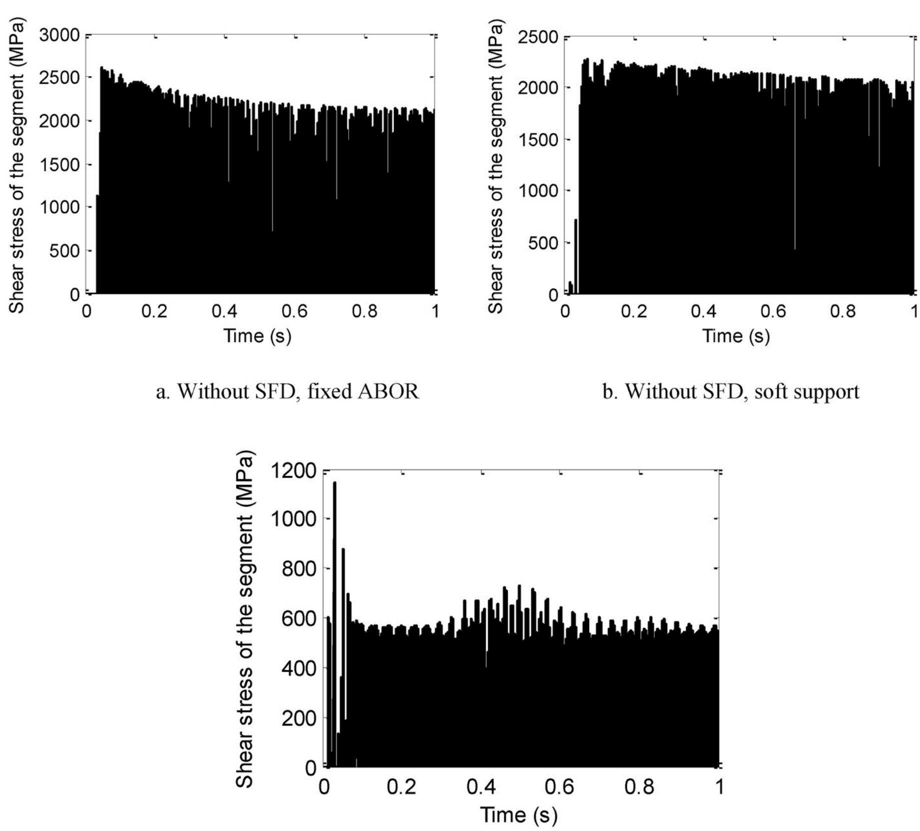

a. Without SFD, fixed ABOR

b. Without SFD, soft support

c. with SFD

Fig. 17. Contact stress during rotor drops.

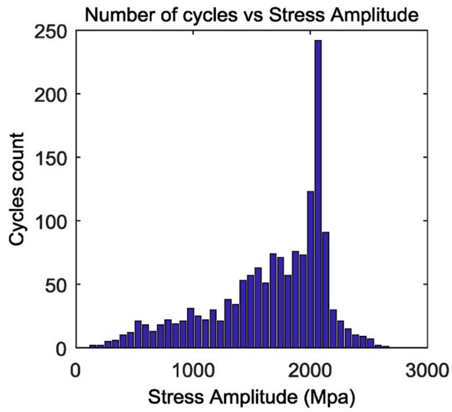

a. Without SFD, fixed ABOR

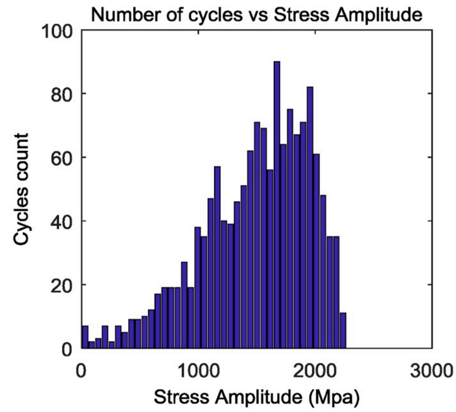

b. Without SFD, soft support

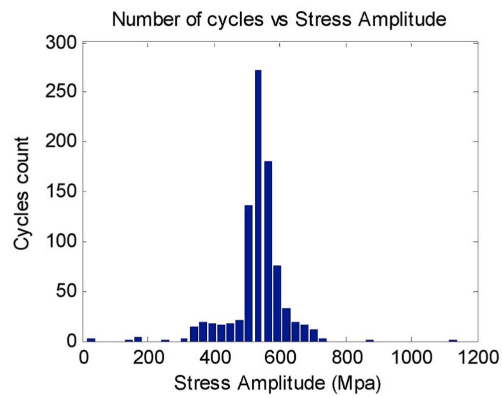

c. with SFD

Fig. 18. Stress cycle of the segment of the ABIR with the lowest fatigue life.

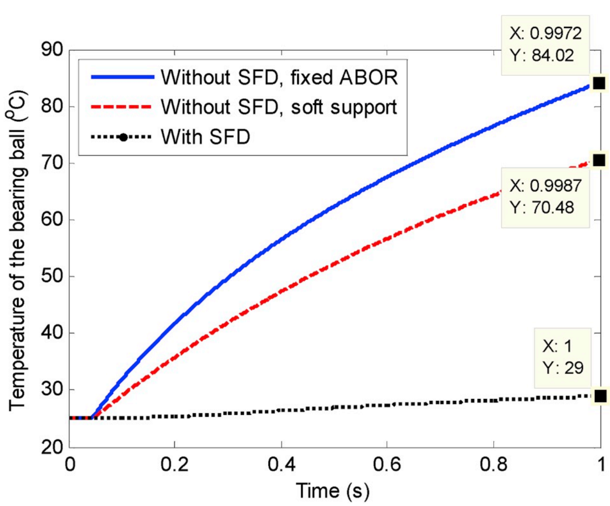

Fig. 19. AB ball temperature after the rotor drop event.

SFD) case includes the squirrel gage stiffness as the support for the AB. The film clearance of the SFD is represented by the symbol "FC".

Fig. 20 shows that the BW is eliminated when the SFD clearance is 0.254 mm and 0.19 mm, but is strong with a 0.127 mm clearance and is severe with a 0.381 mm clearance. This reveals that an optimal SFD oil film clearance range exists outside of which damaging BW may occur during a drop event. Fig. 21 shows the AB "penetration" vs. SFD oil film clearance. Penetration here refers to the radial excursion of the shaft beyond the unloaded clearance circle of the AB. The maximum penetrations are reduced after including the SFD, however, when the clearance is 0.381 mm, the rotor will still impact the AMB due to backward whirl. There is no backward whirl when the SFD oil film clearance is 0.254 mm and 0.1905 mm. The penetration is the smallest when the clearances is 0.127 mm.

The normal contact forces with different SFD clearances are shown in Fig. 22.

The normal contact forces are seen to be much smaller and decay much quicker with a properly designed SFD included. The normal contact forces are the smallest when the SFD clearance is 0.254 mm due to the elimination of backward whirl. Vance's [16] approximate formula for SFD damping coefficients is inversely proportional to the cubic power of the SFD clearance, so that damping will decrease quickly as the clearance is increased. So when the clearance is 0.381 mm the damping provided by the SFD is too small to prevent BW. Alternatively the 0.127 mm clearance yields too large of damping which tends to increase the contact force and reduce energy dissipation (see Fig. 23).

Fig. 24 shows the AB has the highest fatigue life measured in terms of "drop events to failure" when the SFD clearance is 0.19 mm. This results in spite of the maximum normal contact force for the 0.19 mm clearance SFD being slightly larger than for the 0.254 mm clearance SFD. The reason is explained in Fig. 25, which shows the stress cycles of the ABIR segment with the lowest fatigue lives. Though the maximum contact forces are similar, the stress distributions for the 0.19 mm clearance SFD has less cycles at higher stress than the 0.254 mm clearance SFD, which provides a better fatigue life by (56) and (57).

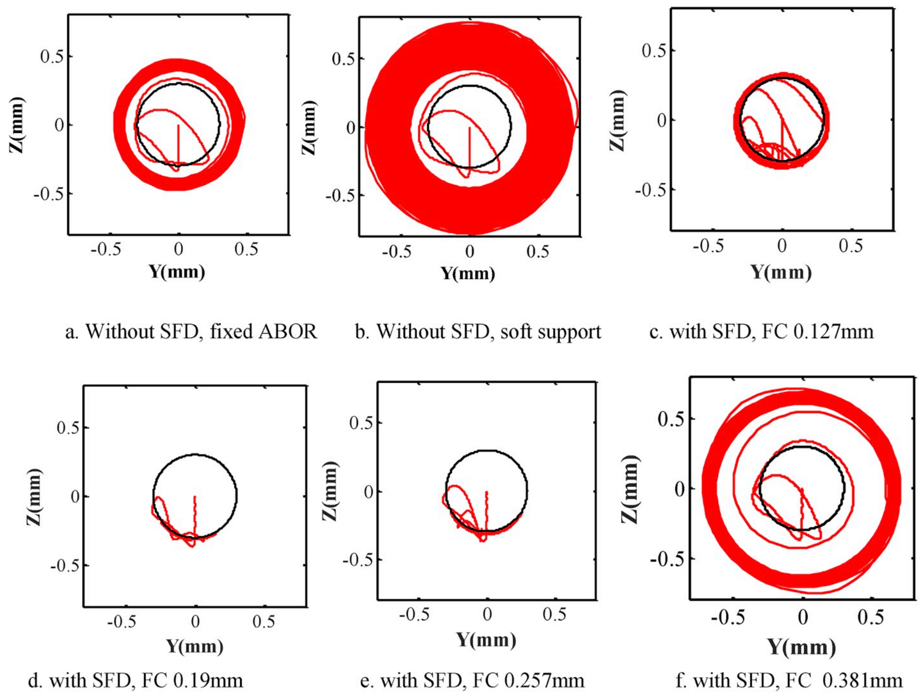

Fig. 20. Rotor orbit with different SFD clearances, considering fluid inertia effect.

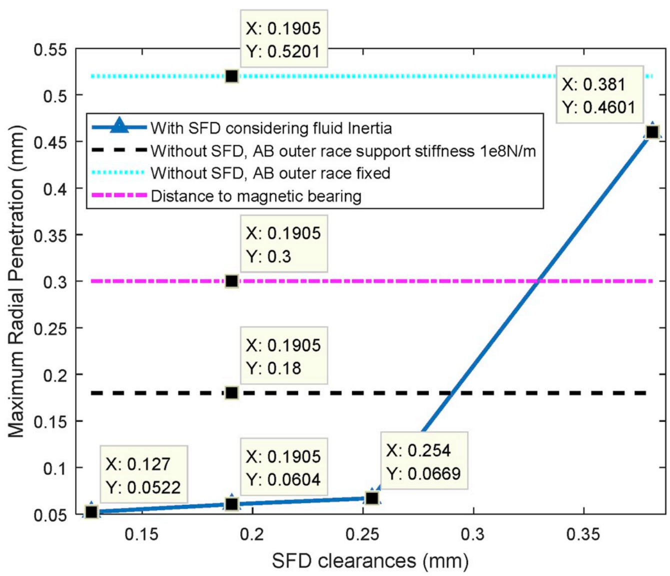

Fig. 21. Maximum penetration with different SFD clearances.

10. Effects of fluid inertia

Previous papers have addressed the subject of impulse loads on hydrodynamic bearings and SFDs for conventional, non-AB type applications, including the effects of fluid inertia. Tichy et al. [17] studied impulse load effects on hydrodynamic journal bearings and concluded that fluid inertia has the effect of reducing predicted vibration amplitudes, while possibly causing abrupt peaks in the vibration waveform. San Andres et al. [18] investigated the response of a SFD-elastic structure system to consecutive impact loads and determined that neglecting fluid inertia results in predicted motions about 50% larger in amplitude than their measured counterparts [18]. These papers demonstrated the effects that including fluid inertia has in reducing predicted vibration amplitudes for impulsive loads. Papers on rotor drops on AB's including SFDs modeled with fluid inertia effects have not previously appeared in the literature. The following results provide comparisons of predicted rotor drop response with and without fluid inertia effects. The SFD clearance is varied from 0.127 mm to 0.381 mm and the effective clearance ratio of the groove land is selected to be 20, which is the same as in the section above.

Fig. 26 shows the predicted rotor drop response orbits for the cases of without the SFD, and with 0.127, 0.254 and 0.381 mm clearance SFD models. Fluid inertia is neglected in all SFD cases. Comparison of Fig. 20 (with fluid inertia) and Fig. 26 (without fluid inertia) show that including fluid inertia has the effect of causing BW for the 0.127 mm clearance case and slightly decreasing the severity of the BW for the 0.381 mm clearance case.

Fig. 27 compares the maximum radial penetration of the orbit beyond the unloaded AB clearance circle, with and without fluid inertia included in the model. Fluid inertia is seen to cause a slight decrease in the maximum radial penetration for the 0.19 mm, 0.254 and 0.381 mm clearance cases. This follows the trend established in Ref. [17] of decreased vibration amplitude resulting from including fluid inertia in the SFD oil film model. This trend is contradicted by the 0.127 mm clearance results though in which case the vibration is higher when fluid inertia is included. This results from the presence of BW for the "with fluid inertia" case and the absence of BW for the "without fluid inertia" case. One plausible explanation for the presence of BW for the "with fluid inertia" case is that the fluid inertia impedes the motion of the outer race as the inner race is initially impacted by the rotor. This increases the contact force between the inner race and the rotor which in turn increases the tangential contact force, leading to BW.

Fig. 28 shows the predicted contact force between the shaft and the AB inner race vs. time for the no SFD and the with SFD cases, and with the SFD model that neglects fluid inertia. Fig. 29 shows a comparison of the "with" and "without fluid inertia" model results for the maximum contact forces vs. SFD clearance. These figures show that there is still an optimal clearance existing even if the fluid inertia effect is not considered. Additionally, it can be seen that when the fluid inertia is not included, the contact forces are under-estimated. It is plausible that the fluid inertia can act to resist the movement of the AB outer race resulting in higher contact forces than predicted with a model that neglects fluid

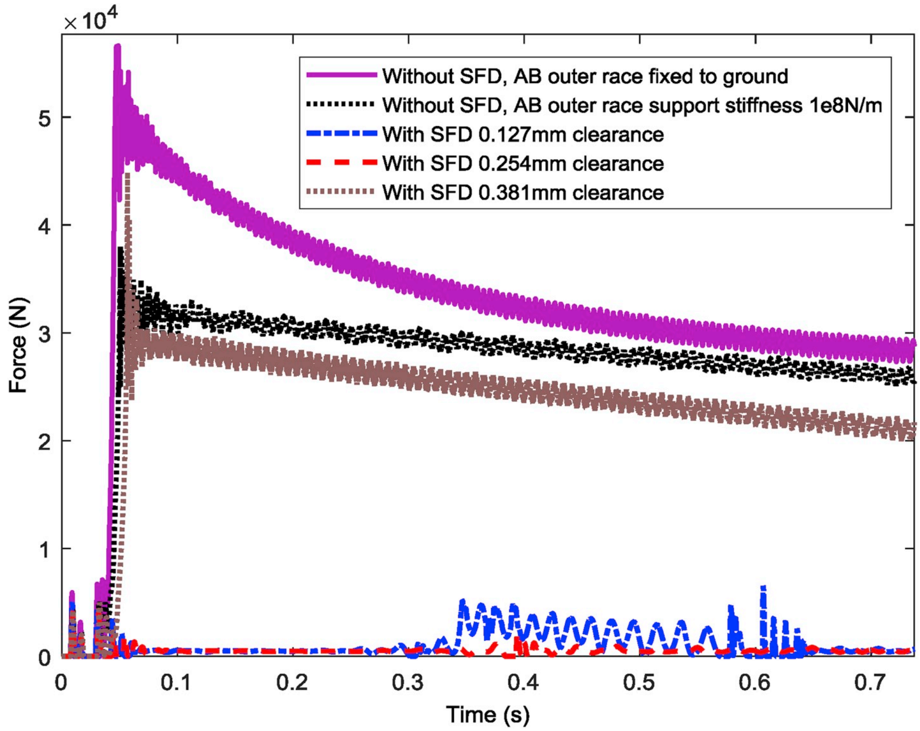

Fig. 22. Normal contact force with different SFD clearances and including fluid inertia.

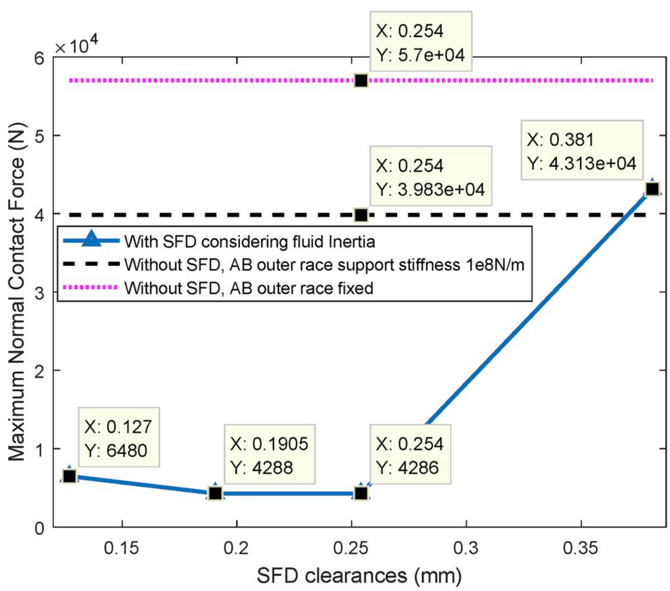

Fig. 23. Maximum normal contact forces with different SFD clearances.

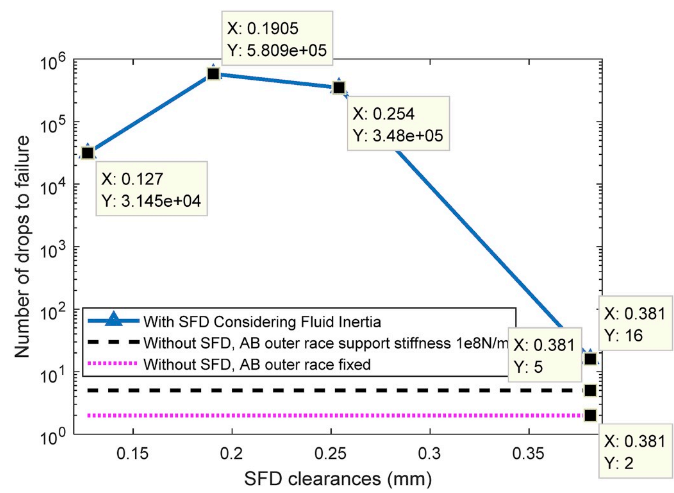

Fig. 24. Fatigue lives of the AB with different SFD clearances.

inertia. The higher contact forces will result in higher friction forces, which may cause BW. This explains why BW whirl occurs in the 0.127 mm clearance case only when fluid inertia is included.

The contact force between the rotor and the AB is mainly caused by the centrifugal force from the high-frequency backward whirl of the rotor. This force is much higher than the impact force during bouncing. That is why the radial penetration becomes larger after including the SFD fluid inertia when the SFD clearance is 0.127 mm. Fig. 30 shows the ball temperature increment with and without the fluid inertia. The temperature is seen to increase as a result of including fluid inertia effects in the SFD model.

Fig. 31 shows the number of drops to AB race failure “with” and “without” considering fluid inertia effects in the SFD model. This shows that AB fatigue life predictions become higher when fluid inertia is neglected. This results since the contact force increases as a result of including fluid inertia in the model which tends to resist movement of the AB outer race. The predicted number of drops to failure for both approaches are very high considering the required number of drops for an actual machine.

11. Summary, conclusions and future work

The central contribution of the theoretical work is an investigation of the potential benefits of installing a squeeze film damper in the auxiliary bearing AB system for a magnetic bearing. The benefits were then demonstrated to be very favorable if the SFD is properly designed for the AB application. The subsidiary contributions include the use of a high

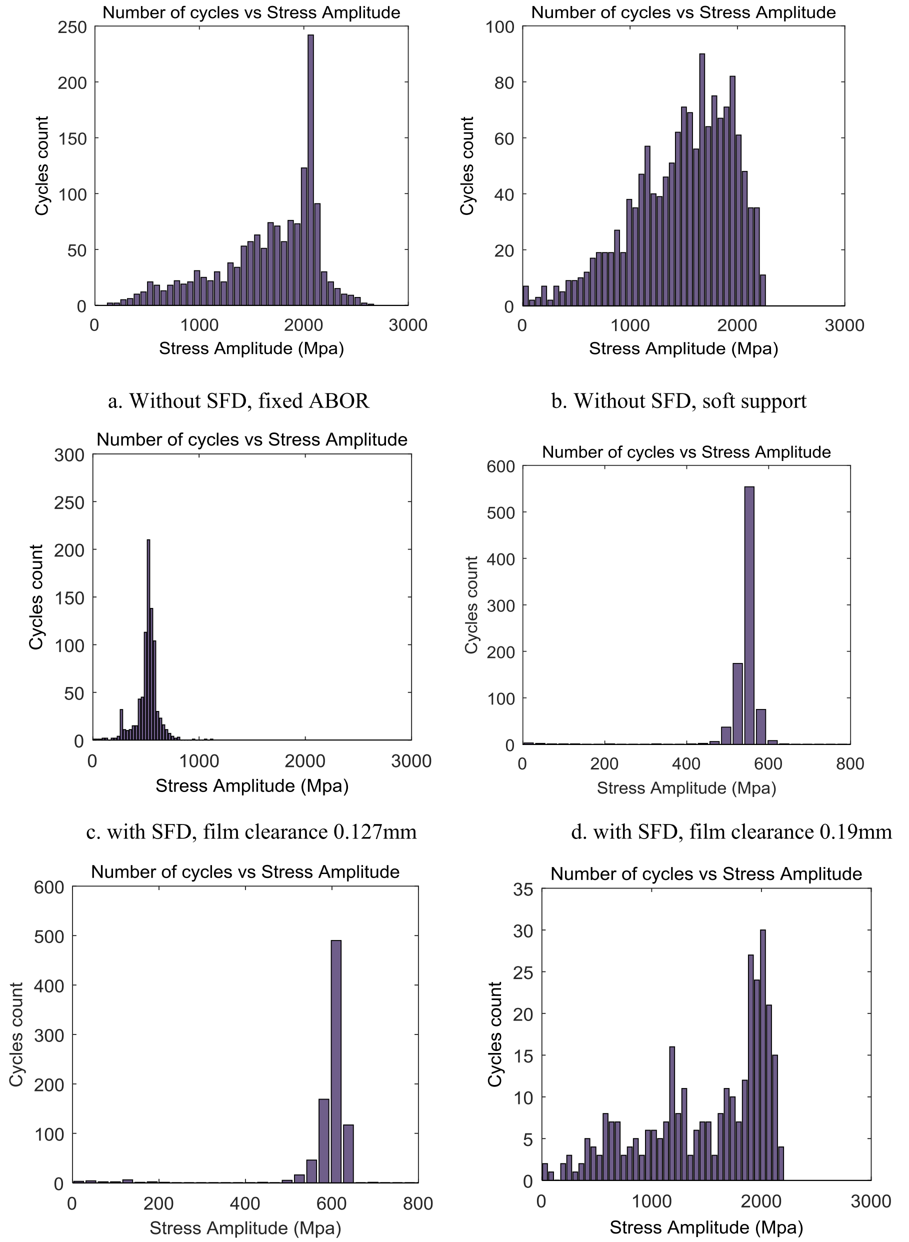

a. Without SFD, fixed ABOR

b. Without SFD, soft support

c. with SFD, film clearance 0.127mm

d. with SFD, film clearance 0.19mm

e. with SFD, film clearance 0.254mm

f. with SFD, film clearance 0.381mm

Fig. 25. Stress cycle of the segment of the ABIR with the lowest fatigue life.

fidelity SFD model, and the evaluation of AB life with and without the SFD, and vs. SFD design parameters. It is notable that.

1. No prior publications included the fluid inertia effect in the model of an AB SFD, designed to suppress transient rotor drop vibrations of a magnetic bearing MB supported rotor.
2. The simulation results indicate that the fluid inertia effect will increase the rotor drop contact force, and therefore reduce the bearing fatigue life, since it tends to resist movement of the AB outer race. This is a valuable observation for designers of MB AB systems that employ SFD.
3. The methodology of judging AB SFD effectiveness by evaluating AB fatigue life employing a Rainflow counting method is a novel contribution of the paper.
4. Helpful guidelines for selecting SFD clearance for AB applications are contributed by the paper. The guidelines are based on the parametric study conducting in the paper.

Detailly, in this study, a high fidelity model for the sudden rotor drop onto an AB with an integrated SFD has been presented. The ball bearing AB model has detailed features including thermal growths, and race and ball motions, forces and deformations. The SFD forces are determined from a finite element based solution of Reynolds equation for film pressure including the fluid inertia effects. The shaft model is composed of Timoshenko beam finite elements including gyroscopic moments. The SFD clearance is varied in the study along with including or neglecting fluid inertia forces in the SFD.

Some conclusions drawn from the simulations include:

An optimal SFD clearance exists for reducing vibrations and contact forces during the drop event and for increasing the AB life. For the four SFD clearances considered, a 0.254 mm clearance resulted in the minimum maximum normal contact force. An explanation for optimal clearance utilizes Vance's [16] approximate formula for SFD damping coefficient, which shows an inverse proportionality to the cubic power of the SFD clearance. The damping rapidly reduces when the clearance

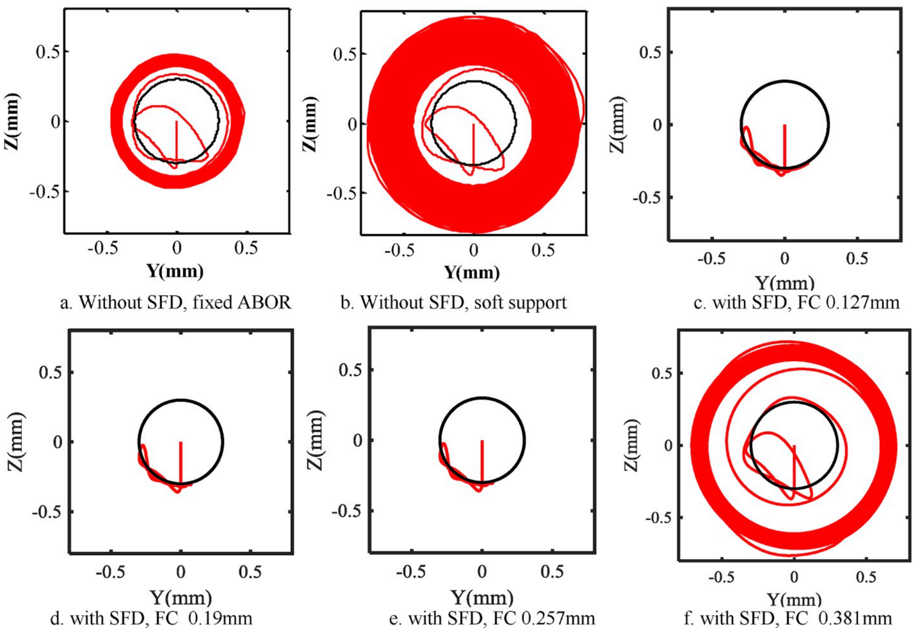

Fig. 26. Rotor orbit with different SFD clearances, neglecting fluid inertia effect.

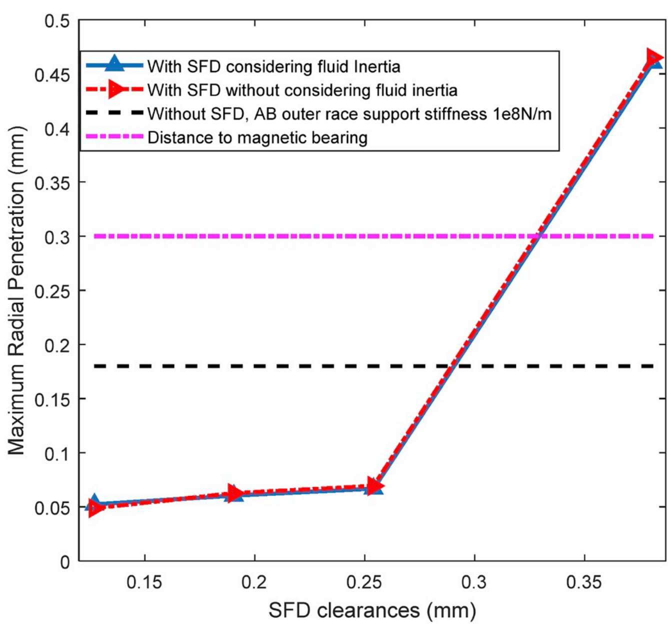

Fig. 27. Maximum radial penetration of the unloaded AB clearance circle.

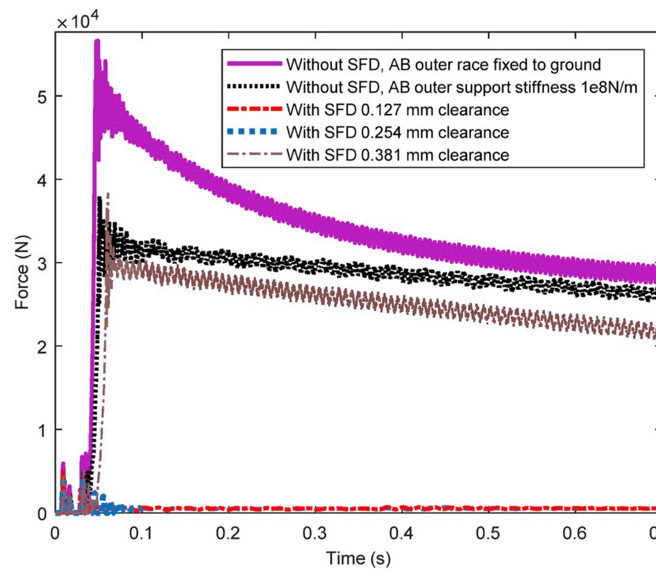

Fig. 28. Normal contact force with different SFD clearances and neglecting fluid inertia.

increases so the damping becomes too small to prevent backward whirl when the SFD clearance reaches 0.381 mm. Conversely, excessively decreasing the clearance will cause the damping to become too large, effectively stiffening the AB support resulting in larger contact forces. Thus with the excessive damping backward whirl may occur but will decay quickly, and high contact forces may result.

Including fluid inertia in the SFD model causes an increase in the predicted contact forces. This also causes backward whirl for the 0.127 mm clearance case, resulting in high contact forces and reduced fatigue life. Therefore, it is important to include fluid inertia in the SFD model to avoid overestimating AB life based on race fatigue.

For the fatigue life calculation of this paper, please note the life prediction is only for the race material and does not include other modes of failure. In addition, the 10^6 cycle life cases, shown in Fig. 30, involve only a relatively low number of load cycles, with relatively low contact pressures (<600 MPa). This is well below the failure line of the SN curve for the race material AISI-52100, as shown in Fig. 11. The main take away point from the life prediction study is that the race fatigue failure can probably be ignored, if the SFD is properly designed to eliminate backwards whirl. This point is supported by considering the drop event orbits in Fig. 19.

The authors appreciate that there is always a need for more experimental results and plan to conduct MB AB SFD tests in the future.

For the present, the high fidelity SFD model with the fluid inertia effect was validated by the test data from Delgado et al. as shown in Fig. 3. The correlation has shown the SFD model itself is reliable.

Utilizing this validated starting point, the paper explored how SFDs can benefit MB AB applications, and how the fluid inertia effect is important to include in a model when designing a SFD for MB AB

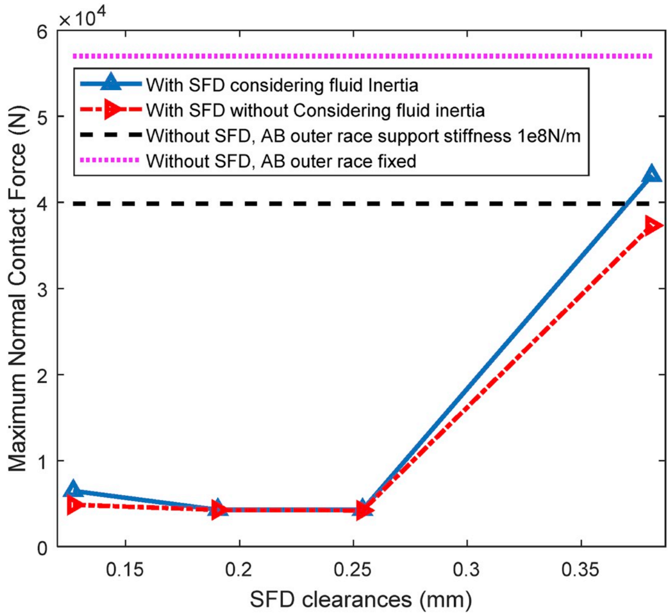

Fig. 29. Maximum normal contact force vs. SFD clearance.

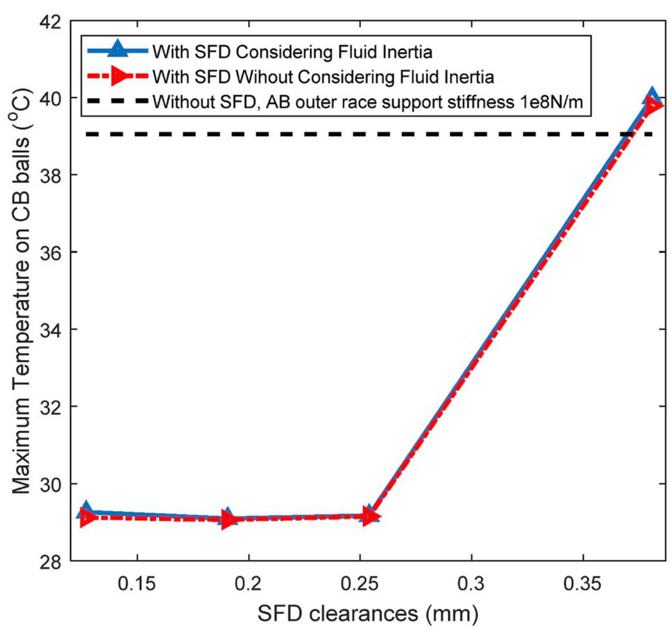

Fig. 30. The maximum temperature of the auxiliary bearing balls.

applications. The MB AB application for a SFD is unique in the sense of

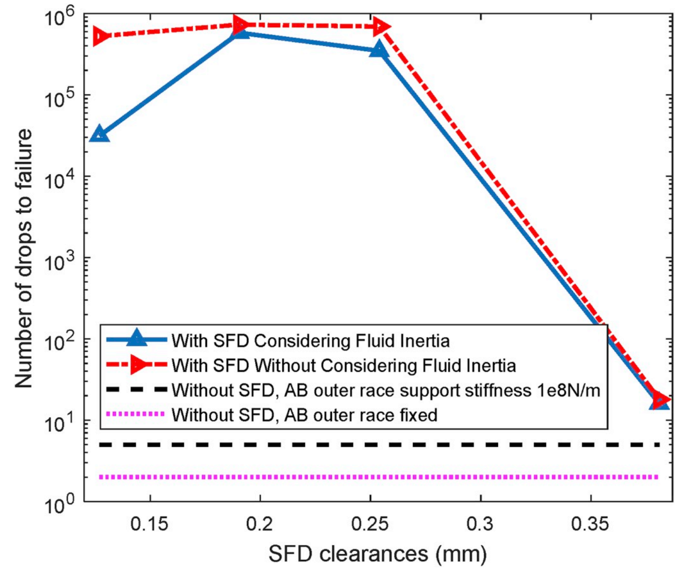

Fig. 31. Number of rotor drops to AB failure.

the suddenly applied transient loading of the SFD.

12. Statement of originalities

1. Installing a high fidelity grooved squeeze film damper model considering the fluid inertia effect along with the high fidelity elastic-thermal coupled ball bearing type auxiliary bearing model for the rotor drop transient simulation.
2. Investigate how the fluid inertia effect influences the rotor drop behavior, etc. Contact force, temperature variation, and bearing fatigue life.
3. Investigate how the film thickness of the squeeze film damper influences the rotor's transient behavior. etc. Contact force, temperature variation, and bearing fatigue life.

Acknowledgment

This research was supported by the Turbomachinery Research Consortium (TRC) at Texas A&M University.

Nomenclature

SFD	Squeeze Film Damper
h_i	Film clearance in the *i*th SFD groove
μ	SFD oil viscosity
$\underline{N}$	Shape function of the triangular element
μ_r	Friction coefficient between the rotor and the auxiliary bearing inner race
AMB	Active Magnetic Bearing
AB	Auxiliary Bearing
ABIR	Auxiliary Bearing inner race
ABOR	Auxiliary Bearing outer race

τ_0	Orthogonal Shear Stress
T_{dl}	Auxiliary Bearing Drag Torque
BW	Backward Whirl
FC	Film Clearance

References

[1] Gelin A, Pugnet JM, Hagopian JD. Dynamic behavior of flexible rotors with active magnetic bearings on safety auxiliary bearings. In: Proceedings of 3rd inernational conference on rotor dynamics; 1990. Lyon, France.
[2] Ishii T, Kirk RG. Transient response techique applied to active magnetic bearing machinery during rotor drop. ASME J Vib Acoust 1996;118:154–63.
[3] Sun Guangyong, Palazzolo Alan, Provenza A, Montague G. Detailed ball bearing model for magnetic suspension auxiliary service. J Sound Vib 2004;269(3):933–63.
[4] Sun Guangyong, Palazzolo Alan. Rotor drop and following thermal growth simulations using detailed auxiliary bearing and damper models. J Sound Vib 2006;289(1):334–59.
[5] Jung gu Lee, Palazzolo Alan. Catcher bearing life prediction using a rainflow counting approach. J Tribol 2012;134(3):03301.
[6] Swanson EE, Kirk RG. AMB rotor drop initial transient on ball and solid bearings. In: Proceeding of magnetic bearing; 1995.
[7] Swanson EE, Kirk RG. Test results and numerical simulation of AMB rotor drop. In: AMB ROtor drop initial transient on ball and solid bearings; 1995.
[8] Kang Xiao, Palazzolo Alan. Dynamic and thermal analysis when rotor drop onto the sleeve type Auxiliary bearings. J Eng Gas Turbines Power 2018;140. 022501-15.
[9] Wilkes Jason, Moore J, Ransom D, Vannini G. An improved catcher bearing model and an explanation of the forward whirl/whip phenomenon observed in active magnetic bearing. ASME J Eng Gas Turbines Power 2013;136.
[10] Zhu Y. Dynamic analysis of auxiliary bearing with elastic ring. J Mech Eng 2011;47.
[11] Delgado A, San Andres L. A model for improved prediction of foce coefficients in grooved squeeze film dampers and oil seal rings. J Tribol 2010;132. 032202-1-12.
[12] Matthew T. Caprio, brian murphy, john herbst, "spin commisioning and drop tests of a 130 kW-hr composite flywheel. In: Proc. 9th int. Symp. Magnetic bearings; 2004. Lexington, KY.
[13] Harris TA. Rolling bearing analysis. fifth ed. New York: Wiley; 2006.
[14] Olejnik Pawel. Modeling, analysis and control of dynamical systems with friction and impacts. World Scitific; 2018.
[15] Raje N, Sadeghi F. Statistical numerical modeling of sub-surface initiated spalling in bearing contacts. J Eng Tribol 2009;223(6):849–58.
[16] L. S. Andres, "Squeezze film dampers: operation, models and technical issues, Lecture Note," [Online]..
[17] Tichy John, Bou-Said Benyebka. Hydrodynamic lubrication and bearing behavior with impulsive loads. Tribol Trans 1990;34:505–12.
[18] San Andres Luis, Sung-Hwa Jeung. Response of a squeeze film damper-elastic structure system to multiple and consecutive impact loads. J Eng Gas Turbines Power 2016;128.